

Evolution of Microstructure and Texture During Deformation and Recrystallization of Heavily Rolled Cu-Cu Multilayer

K.S. SURESH, A.D. ROLLETT, and SATYAM SUWAS

A Cu-Cu multilayer processed by accumulative roll bonding was deformed to large strains and further annealed. The texture of the deformed Cu-Cu multilayer differs from the conventional fcc rolling textures in terms of higher fractions of Bs and RD-rotated cube components, compared with the volume fraction of Cu component. The elongated grain shape significantly affects the deformation characteristics. Characteristic microstructural features of both continuous dynamic recrystallization and discontinuous dynamic recrystallization were observed in the microtexture measurements. X-ray texture measurements of annealing of heavily deformed multilayer demonstrate constrained recrystallization and resulted in a bimodal grain size distribution in the annealed material at higher strains. The presence of cube- and BR-oriented grains in the deformed material confirms the oriented nucleation as the major influence on texture change during recrystallization. Persistence of cube component throughout the deformation is attributed to dynamic recrystallization. Evolution of RD-rotated cube is attributed to the deformation of cube components that evolve from dynamic recrystallization. The relaxation of strain components leads to Bs at larger strains. Further, the Bs component is found to recover rather than recrystallize during deformation. The presence of predominantly Cu and Bs orientations surrounding the interface layer suggests constrained annealing behavior.

DOI: 10.1007/s11661-013-1749-0

© The Minerals, Metals & Materials Society and ASM International 2013

I. INTRODUCTION

METALLIC multilayers are known to possess better mechanical properties compared with monolithic materials.^[1-4] In addition to the dislocation pile up at the grain boundary, as occurring in conventional bulk polycrystalline materials for strengthening, multilayers possess an additional constraint for either confined layer slip,^[5] or the dislocation movement across the interface. Hence, the increase in strength is contributed by grain size refinement as well as the interface spacing of the lamellae. The synthesis methods available for multilayers include thin film deposition techniques^[6-10] and roll bonding processes.^[11-15] The response of these types of multilayer composites to large strain plastic deformation has been studied by characterizing the evolution of hardness, texture, and microstructure.^[7,9-13] However, most of these studies focused on dissimilar materials that demonstrate additional hardening behavior pertaining to modulus mismatch, lattice incoherence, and chemistry. Hence, the deformation characteristics and evolution of texture in such dissimilar multilayer

composites is quite complex. Dislocation transfer across an interface (grain boundary) in a monolithic multilayer is much easier compared with the dissimilar multilayer, and deformation mechanisms could be easily predicted based on the analysis of microstructure and texture.

Copper having a medium stacking fault energy (SFE) has been well studied in terms of the evolution of microstructure and texture during conventional rolling as well as accumulative roll bonding (ARB).^[16-18] However, the response of ARB-processed Cu-Cu multilayers to further deformation behavior and their texture evolution has not been studied, and so it is an ideal candidate to study post-deformation characteristics. It has also been reported that failure of ARB-processed samples typically occurs at the poorly bonded interface.^[12,13,19,20] In general, the last bonded interface acts as a prominent location for delamination because of its weaker bonding. Such multilayers could therefore be strengthened during further rolling through proper bonding and grain refinement. Although grain refinement leads to higher strengthening, the resulting material exhibits limited ductility. A bimodal grain size distribution with a large area fraction of $\Sigma 3$ boundaries shows enhanced ductility with slight reduction in strength.^[21-23] Along with better mechanical properties, high-purity Cu-Cu multilayer having excellent electrical conductivity might be useful in the semiconductor industry as interconnects.^[24] The presence of a high fraction of $\Sigma 3$ boundaries provides both better mechanical properties and higher resistance to electro-migration.^[25] The annealing of rolled Cu results in increased content of $\Sigma 3$ boundaries.^[26] Higher fractions of twin

K.S. SURESH, formerly Ph.D. Student with Department of Materials Engineering, Indian Institute of Science, Bangalore 560012, India, is now Post Doctoral Researcher with High Temperature Materials Unit, National Institute for Materials Science, Tsukuba, Ibaraki 3050047, Japan. A.D. ROLLETT, Professor, is with the Department of Materials Science and Engineering, Carnegie Mellon University, 5000 Forbes Avenue, Pittsburgh, PA 15213. SATYAM SUWAS, Associate Professor, is with the Department of Materials Engineering, Indian Institute of Science. Contact e-mail: satyamsuwas@materials.iisc.ernet.in

Manuscript submitted August 27, 2012.

Article published online May 7, 2013

boundaries in Cu Damascene lines were found to improve the electro-migration performance of interconnects.^[27,28] So, Cu multilayers with a high twin fraction could serve both structural and functional roles.

The current study is aimed at understanding the evolution of microstructure and texture during large strain deformation and annealing of an ARB-processed high-purity Cu-Cu multilayer through conventional rolling. Also, the effect of the interface layer on grain refinement and grain growth during annealing will be addressed. To understand the deformation mechanism, crystal plasticity simulations were employed to simulate the experimental texture and thereby account for the presence and strength of texture components.

II. MATERIALS AND METHODS

A. Experimental Procedure

1. Processing

A Cu-Cu multilayer was produced by ARB. This method involves the stacking of two high-purity Cu (99.99 pct) sheets of equal thickness and then the stacked layers were given 50 pct reduction by rolling at 573 K (300 °C). The roll bonded Cu-Cu layers were cut into halves, stacked together and rolled once again to 50 pct reduction. This repetitive rolling process was continued to eight passes. A detailed description of the ARB procedure is given by Suresh *et al.* in Reference 29. At the end of eight cycles of ARB, the Cu-Cu multilayer consists of 256 individual Cu layers and has been subjected to a total strain of 4.8. The eight pass ARB-processed Cu-Cu multilayer was taken as the starting material for the current study. The Cu-Cu multilayer was further cold rolled to 25 (5.6), 50 (6.2), 75 (6.9), 87 (7.7), and 93 pct (8.4) reduction (The cumulative von-Mises equivalent strains for each rolling reduction are provided in the braces). The deformed samples were vacuum annealed at 523 K (250 °C) for 30 minutes.

2. Characterization

All the deformed and annealed samples were metallographically polished for microstructural observations on the RD-ND cross-section. Microstructure and micro-texture analyses were carried out using TSL™ electron back scattered diffraction (EBSD) detector attached to a FEI-SIRION® field emission gun-scanning electron microscope (FEG-SEM). All the microstructural observations were made on the RD-ND section. The measured data were characterized using TSL-OIM™ 5 software to obtain microstructural information. Regions that contained a minimum of 5 pixels and having a misorientation of 5 deg were considered as separate grains. The grain size was calculated using the linear intercept method. The grain size distributions and other microstructural analyses all included at least 350 grains. The misorientation angle distribution was classified as very low angle boundaries (VLAB) (2 to 5 deg), low angle boundaries (LAB) (5 to 15 deg) and high angle boundaries (HAB) (>15 deg). To evaluate the amount of strain in different grains as well as in different regions of

a single grain, misorientation parameters such as grain orientation spread (GOS), grain average misorientation (GAM) and kernel average misorientation (KAM) maps were calculated. GOS is defined as the average misorientation between each pixel and the average orientation of the given grain. KAM is calculated by defining a Kernel. It is the average misorientation between a pixel at the center of the kernel and all the surrounding first nearest-neighbor pixels. GAM is the average of the KAM values in a given grain. For Bulk X-ray texture measurements, the polished samples were irradiated on the rolling plane with Cu K α radiation and incomplete (111), (200), (220), and (311) pole figures were measured using a Bruker D8-Discover™ X-ray texture goniometer. The orientation distribution function (ODF) was calculated from the measured pole figures using the Arbitrary Defined Cell (ADC) method^[30] as employed in the Labotex™ 3.0 software. The volume fraction of texture components was determined with a 10 deg spread in Gaussian. A list of all the important texture components with {hkl}<uvw> orientations and their exact locations in the Euler space is given in Table I. Transmission electron microscopy (TEM) investigations were made on the RD-ND section of the sample, using standard cross section TEM techniques. After standard metallographic polishing, electron transparent regions were created using Gatan Precision Ion Polishing System (PIPS). A Field Emission Gun (FEG) FEI-Tecna F-30 TEM was used for microstructural analysis.

B. Simulation Approach

The viscoplastic self-consistent (VPSC) model^[31] was used to simulate the evolution of texture during rolling of Cu multilayer and thereby it was also used to understand the origin and transition of certain significant texture components. In the VPSC model, the slip rate $\dot{\gamma}^s$ is related to the grain stress σ by the following relation:

$$\dot{\gamma}^s = \dot{\gamma}_0 \left| \frac{m^s : \sigma}{\tau_c^s} \right|^{n_s} \text{sign}(m^s : \sigma)$$

where $\dot{\gamma}_0$ is the normalizing strain rate, m^s Schmidt tensor, τ_c^s slip resistance for slip system and n_s the strain rate sensitivity exponent. Based on the above equation slip system s is activated when the resolved shear stress $m^s : \sigma$ approaches τ_c^s . The VPSC model accounts for the

Table I. Euler Angles for the Various Texture Components

Component	{hkl}<uvw>	ϕ_1	ϕ	ϕ_2
Copper (Cu)	{112}<111>	90	35	45
Brass (Bs)	{110}<112>	35	45	90
S	{123}<634>	59	37	63
Cube	{001}<100>	0	0	0
RD-Cube	{013}<100>	0	22	0
Goss	{011}<100>	0	45	0
BR	{236}<385>	80	31	35
R	{124}<211>	57	29	63
Dillamore	{4 4 11}<11 11 8>	90	27	45

initial texture and texture evolution associated with the shear rate, as well as allows the strain path followed by each grain to vary from the average according to its interaction with the polycrystal as a whole. Geometrical hardening (or softening) is taken into account as a

consequence of orientation change. A more detailed description of the model is given in Reference 32. For the current study, the ODF calculated from the X-ray measured pole figures of the starting material was discretized into a set of 2000 individual orientations and used as the initial texture. The hardening parameters for the octahedral $\{111\}\langle 110\rangle$ slip systems corresponding to Cu single crystal is given in Table II followed by Tu in Reference 28 Based on the microstructural observation from EBSD, the grain aspect ratio 1:0.125:0.125 was used for texture prediction. Texture was simulated with the n^{eff} approach for the interaction between each grain and the homogeneous medium.^[32]

Table II. Voce Hardening Parameters Used in the Texture Simulation of VPSC Corresponding to $\{111\}\langle 110\rangle$ Slip System in Cu

τ_0	τ_1	θ_0	θ_1
10	2	10	5

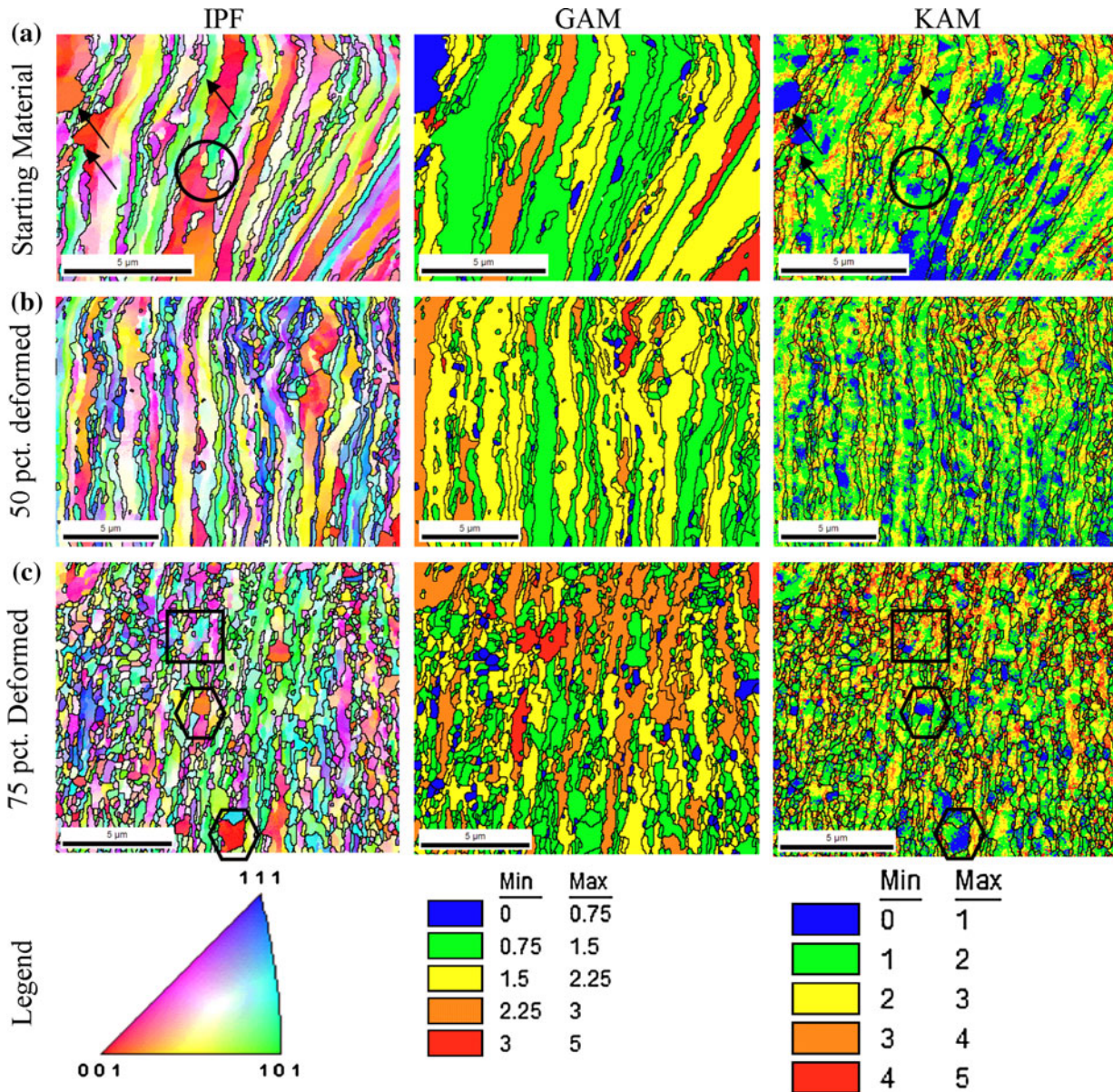


Fig. 1—Inverse Pole figure maps, grain average misorientation maps, and Kernel average misorientation maps for the (a) Starting material, (b) 50-pct-deformed, and (c) 75-pct-deformed samples. Arrows denote curved grain boundaries that have high misorientation on the concave side and low misorientation on the convex side. Circled region indicates the formation necking. Hexagon represents low intra-grain misorientation and rectangle high intra-grain misorientation.

III. RESULTS

A. Microstructural Features

In the following sections, the microstructural observations of the as-rolled and annealed multilayers are presented.

1. Microstructure of the deformed samples

Figure 1 shows the EBSD generated microstructures of the multilayers before and after cold rolling in terms of inverse pole figure (IPF), GAM and KAM maps. The starting material (from ARB) exhibits heterogeneous deformation features. The thickness of individual layers as well as the grain size in a particular layer varies significantly. Along with the elongated grains, some equiaxed grains are also present, mostly adjacent to the interlayer interface of the starting material. The fraction of equiaxed grains increases with increasing strain. In the starting material, some parts of a layer have protruded into the neighboring layer. Almost all the interfaces are curved. In Figure 1, the protruded regions have been marked with a black arrow in the IPF and KAM maps for the starting material. The black arrows

denote regions with very low intra-grain misorientation surrounded by a grain boundary for which the surrounding material possesses large orientation gradients. A feature similar to cell structure can also be observed in the KAM map of the starting material, where within a single layer, certain regions have low KAM values and neighboring regions have high KAM values. For all the deformation conditions, the average grain size is large compared with the average layer thickness. Necking was also evident at several locations and one such region is identified with a black circle. Nucleation of new grains is evident in the necks. Similar features are apparent in the IPF maps of the 50- and 75-pct-deformed samples (Figure 1). With increasing strain the layered structure transforms to equiaxed grains having lower KAM values. However, for the 50-pct-deformed sample, most of the equiaxed grains possess large intra-grain misorientation and are located mostly adjacent to the inter-layer interface. After 75 pct rolling reduction, a large fraction of fine equiaxed grains with low KAM values are observed. This sample also contains large grains with different intra-grain misorientation levels. The grain with minimum misorientation is highlighted with

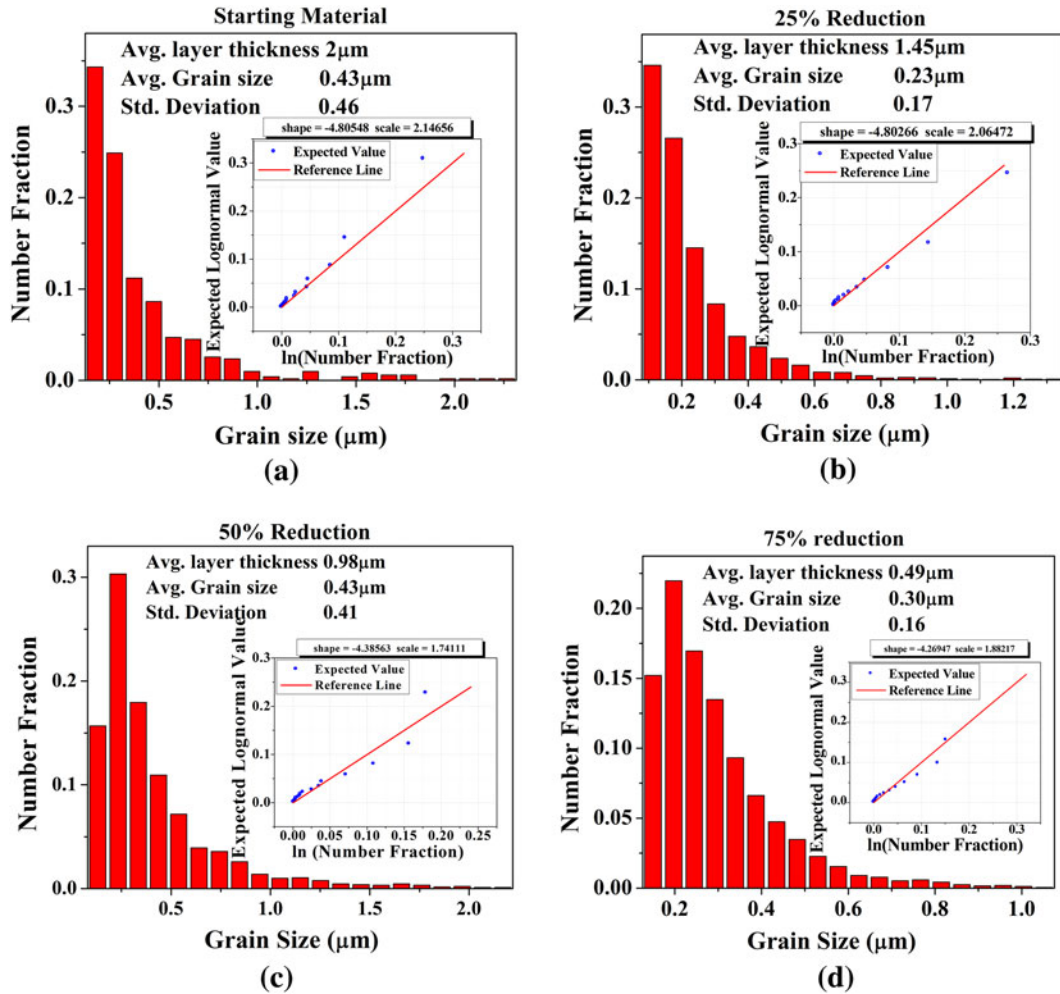


Fig. 2—Grain size distribution for the (a) starting material, (b) 25-pct-deformed, (c) 50-pct-deformed, and (d) 75-pct-deformed Cu-Cu multilayers. Log-normal quantile plots are included as an inset to validate the grain size distribution. Up to 25 pct deformation, the grain size distribution is log-normal beyond which it starts to deviate.

a black hexagon, and a black rectangle for the one with large misorientation. All the marked grains in 75-pct-deformed sample exhibit a grain size of $\sim 1 \mu\text{m}$ which is more than twice the average layer thickness.

To assess the extent of grain refinement, grain size distributions for the deformed samples, along with the starting material, are shown in Figure 2 in terms of number fraction. Additionally, a quantile plot for the cumulative grain size distribution, the average layer thickness, average grain size and standard deviation of grain size are included as an inset in each individual graph. The average grain size initially decreases, then increases after 50 pct deformation, and then decreases again such that the final grain size ($0.30 \mu\text{m}$) is smaller than the initial ($0.43 \mu\text{m}$). For all the samples, a significant fraction of grains is present whose grain size is more than the average layer thickness. In the starting material, as well as during initial stages of deformation, the variation in the grain size distribution is quite large, which can be observed from the standard deviation values provided within each graph. The probability plots, given as the inset for each deformation condition, indicate that the grain size distribution is close to a log-normal distribution for the starting and 25 pct reduction conditions but increasingly deviates with increasing strain (as evident from the deviation of the upper tail

from a straight line). Other microstructural parameters namely, grain aspect ratio, misorientation angle profile, GBCD and GAM distributions are shown in Figure 3. The lamellar structure of the starting material changes to equiaxed grain shape with increase in strain. It is evident from Figure 3(a) that the grain aspect ratio moves toward one with the increase in strain. The misorientation angle distribution is similar for all the samples, with large fractions of VLABs compared with LABs (Figures 3(b) and (c)). With increase in strain the amount of HABs increases. With increase in strain (up to 50 pct deformation), the peak value of GAM distributions shifts toward higher misorientation (Figure 3(d)). Besides the peak shift to a higher value, for 25-pct-deformed sample the standard deviation of GAM distribution is larger than that of the starting material. For 75-pct-deformed samples, the maximum GAM value decreases to a lower value.

2. Microstructure of the annealed samples

IPF and IQ maps of the annealed samples are shown in Figure 4. Both map types exhibit the presence of large fractions of twins and a wide range of grain sizes. Although most of the grains have grown so that they span several layers, the growth is more along the individual layer, leading to elongated grain shapes.

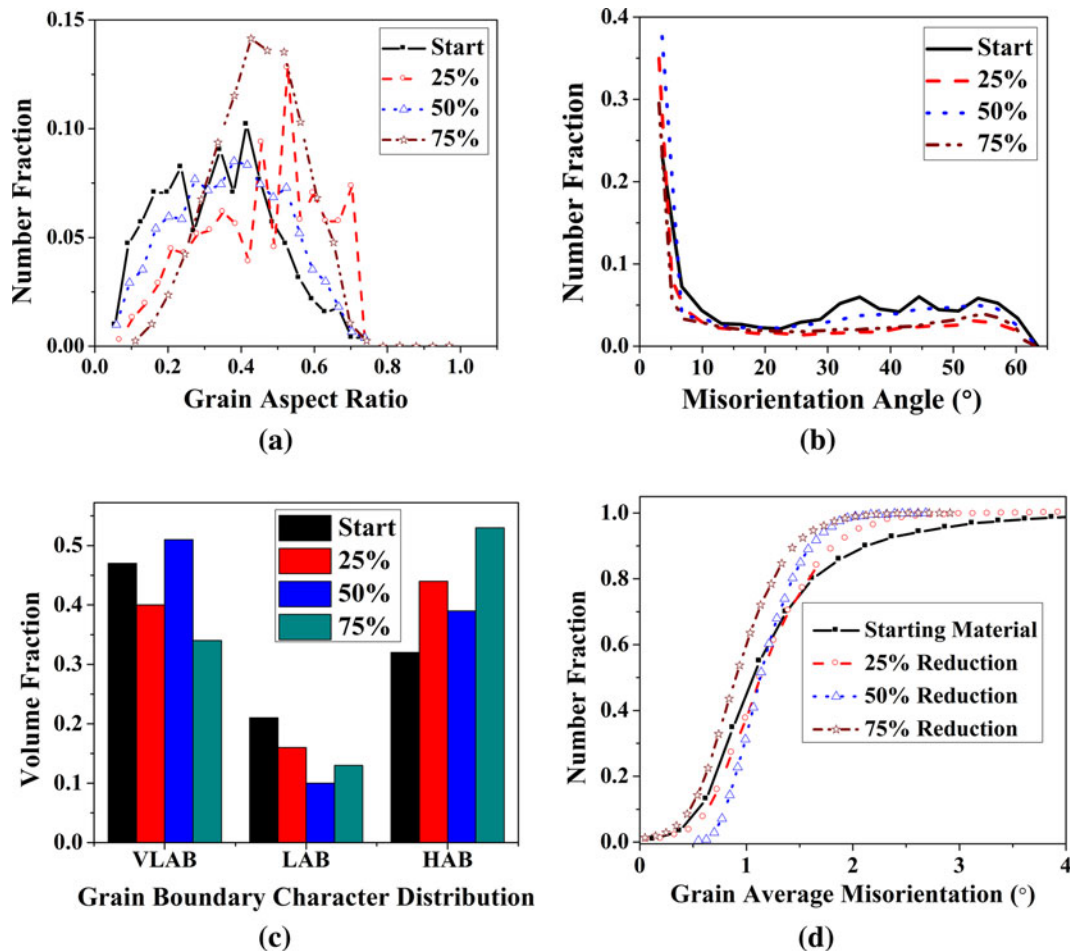


Fig. 3—(a) Grain aspect ratio, (b) misorientation angle, (c) grain boundary character distribution, and (d) cumulative Grain Average Misorientation. With increase in deformation GAR moves toward 1.

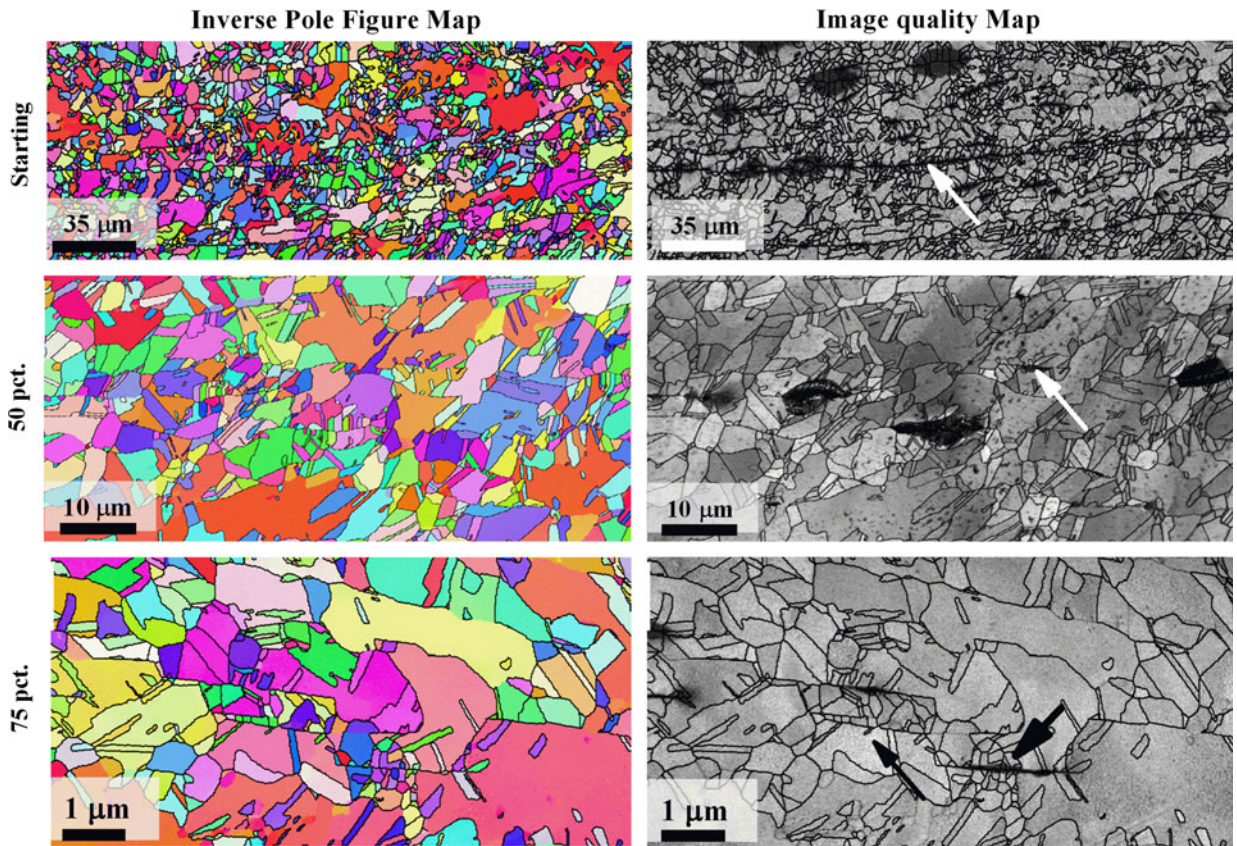


Fig. 4—Inverse pole figure and image quality maps for the deformed multilayer after annealing. Arrow indicates formation of fine grains surrounding the thin oxide region.

A large fraction of fine grains are observed surrounding thin oxide layer along the interlayer interface. Such types of fine grains are more evident in (annealed) starting material. Furthermore, the extent of twin formation is also greater in these regions. The starting material and 25-pct-deformed sample display a unimodal grain size distribution, which after larger deformation changes to a bimodal distribution, Figure 5. The average grain sizes for different conditions show small but expected variations, *i.e.*, the average size increases from the starting material to 25 pct reduction and then drops steadily with increasing reduction; the standard deviations track the average values. The probability plot given as an inset indicates that the grain size distribution follows a log-normal distribution for lower amount of strain, which tends to deviate at larger rolling reductions. Figure 6(a) shows similar distributions of grain aspect ratio for all the annealed samples. The misorientation angle distribution is also similar for all the cases (Figure 6(b)). The 75-pct-deformed sample after annealing has a larger fraction of LABs than any of the other conditions, Figure 6(c). The fraction of coincidence site lattice (CSL) boundaries increases for annealed samples with prior deformation up to 50 pct but drops for 75 pct, presumably because of the increase in LABs. The fraction of high angle boundaries decreases monotonically with increasing prior strain. Among the CSL boundaries only $\Sigma 3$, $\Sigma 9$, and $\Sigma 27$ were found and $\Sigma 3$ is more prominent compared with the other types.

B. Texture Development

1. Texture of deformed materials

The development of deformation textures in severely cold rolled Cu has been characterized by the presence of texture components like Cu, Bs, S, cube, and Goss orientations where S exhibits the maximum intensity followed by Cu and Bs.^[26] The $\phi_2 = 0$ and 45 deg sections of ODF for deformed samples are given in Figure 7. The texture of the starting material reveals relatively weak texture from the ARB process. All the deformed samples exhibit deviation from the conventional observations^[26,33] in terms of presence of stronger Bs component compared with Cu. In addition to the presence of Bs and Cu components, S, cube, and RD-cube components are also strong. More clearly than in the pole figures, the $\phi_2 = 0$ deg sections of ODF show the Cu, Bs, cube, and RD-cube components. The Bs component is concentrated on its ideal location, whereas the Cu component is spread out to enough extent that it overlaps with the Dillamore component. The maximum location of S component is shifted along ϕ_1 by ~ 10 deg from its ideal location (as given in Table I) and is concentrated at the R component. Although the RD-cube component is present in almost all the deformation conditions, its intensity and spread vary markedly. The RD-cube component is spread across Φ from 0 to 30 deg and its spread across ϕ_1 is limited to 10 deg. The recrystallization component of Bs is known as BR.^[26,33]

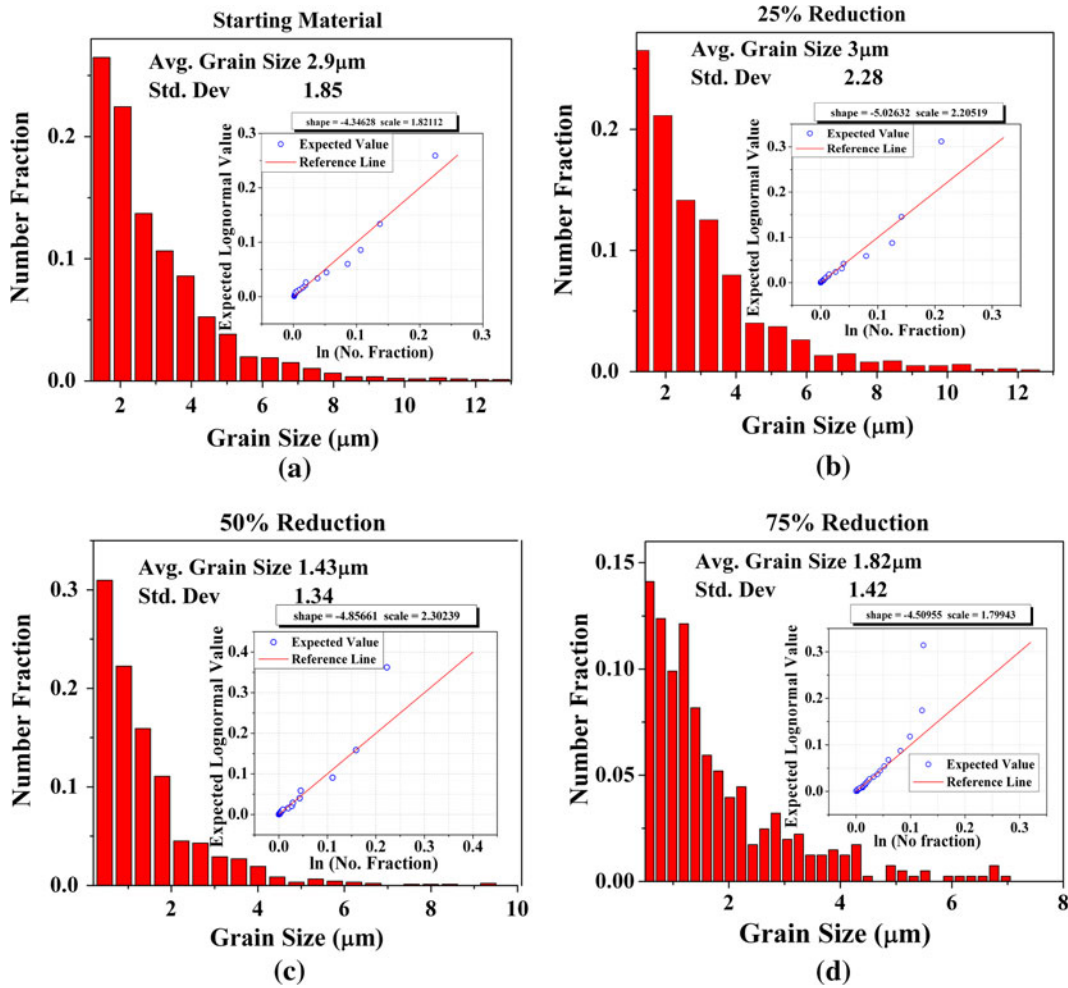


Fig. 5—Grain size distribution for the annealed multilayer corresponding to (a) starting material, (b) 25 pct reduction, (c) 50 pct reduction, and (d) 75 pct reduction. Log normal quantile plots are included as an inset. At lower deformation levels, grain size distribution is log-normal, which deviates at later stages.

Compared with the intensity of cube and RD-cube, BR is weaker in the deformed samples, but is present throughout the deformation process. After 75 pct reduction, the spread of RD-cube as well as its intensity decreases and is mostly concentrated at around $\Phi = 20$ deg. The texture strengthens up to 50 pct reduction, but after that overall texture intensity weakens.

To further characterize the development of various texture components during deformation and their interdependence, the volume fraction of various fcc deformation texture components and the ratio between some important texture components are depicted in Figure 8. The S component possesses the highest volume fraction among all the texture components, which was not evident in β fiber. Similar to the observations in ODF, volume fraction distributions show a higher Bs component compared with Cu in all the deformed samples, and show a maximum at 87 pct reduction. Both Bs and S components increase with deformation. The changes in the volume fraction of Goss and Cu components are not prominent. Similarly, the strengths of the cube and RD-cube components do not vary until 75 pct reduction.

However, after 75 pct reduction, there is a minor decrease in their strength. The ratio of volume fractions of S to Cu shows an analogous behavior to that of Bs to Cu. The variation in the ratio of S to Bs is negligible.

2. Texture of annealed samples

The $\phi_2 = 0, 45,$ and 65 deg sections of ODF for the annealed sample are given in Figure 9. The ODF clearly indicates the presence of strong cube and BR components with negligible amount of Goss. Annealing of the starting material leads to very weak texture compared with the other samples. The cube component is present in all the annealed samples. In contrast to the large variation in the volume fraction of cube component in the deformed samples, annealed materials display less broadening. Annealing of samples deformed up to 50 pct reduction strengthens the overall texture, beyond which the texture slightly weakens and stabilizes. Besides the weakening of texture, some of the deformation texture components are retained for samples that are annealed after 93 pct deformation. To analyze the relative fraction of deformation and recrystallization

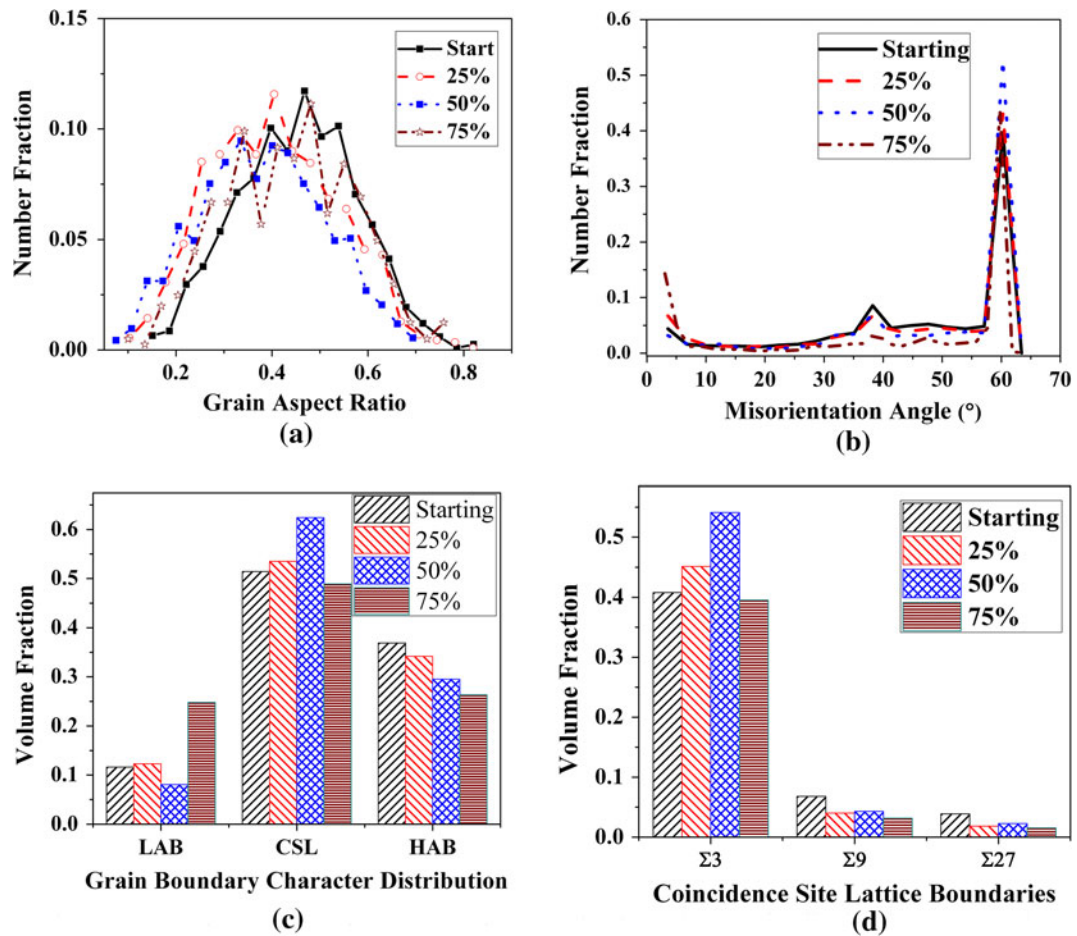


Fig. 6—(a) Grain aspect ratio (GAR), (b) misorientation angle distribution, (c) grain boundary character distribution, and (d) coincidence site lattice distribution for the annealed multilayer. GAR and misorientation angle distribution are similar for all the conditions. HAB fraction slightly decreases with deformation.

texture components in the annealed samples, all the major fcc texture components are plotted in Figure 10. The volume fraction of cube and BR components increases monotonically in annealed samples that have undergone deformation up to 50 pct. Beyond this point, the cube and BR components decrease steadily. The strength of the Bs component decreases to a larger extent after recrystallization compared with the other deformation texture components. The volume fraction of S component also decreased, however, to a limited extent in the annealed condition.

C. Texture Simulation

Orientation distribution functions generated from the VPSC simulations are given in Figure 11(a) for the $\varphi_2 = 0, 45,$ and 65 deg sections for 75 and 93 pct rolling reductions. There is a reasonably good match between the experimentally measured rolling texture (Figure 7) and simulated texture (Figure 11). The average number of active slip systems decreases from 3.2 to 2.4 with increasing strain. The ratios between volume fractions of the major texture components are also similar to the experiments (Figure 8(b)). To understand the origin of the RD-rotated cube and Bs components and their

relation to the cube component, the changes in the cube orientation having a spread of 10 deg were observed during deformation, and the corresponding changes are presented in Figure 11(b). Clearly, during the initial stages of deformation (up to 75 pct rolling reduction), the cube rotates about the RD and later from the RD-rotated cube to Bs orientation (at 93 pct rolling reduction). A similar texture change has also been reported by Hirsch *et al.*^[34] Further, VPSC simulations showed that cube orientations move toward Bs at a faster rate compared with the formation of Cu or S component, essentially because orientations originating at cube pass through or near Bs on their way toward S or Cu.

IV. DISCUSSION

A. General Observations

The microstructural and texture observations presented in Section III lead to the following inferences: (i) occurrence of continuous dynamic recrystallization (CDRX) and discontinuous dynamic recrystallization (DDRX) during deformation, (ii) absence of twinning

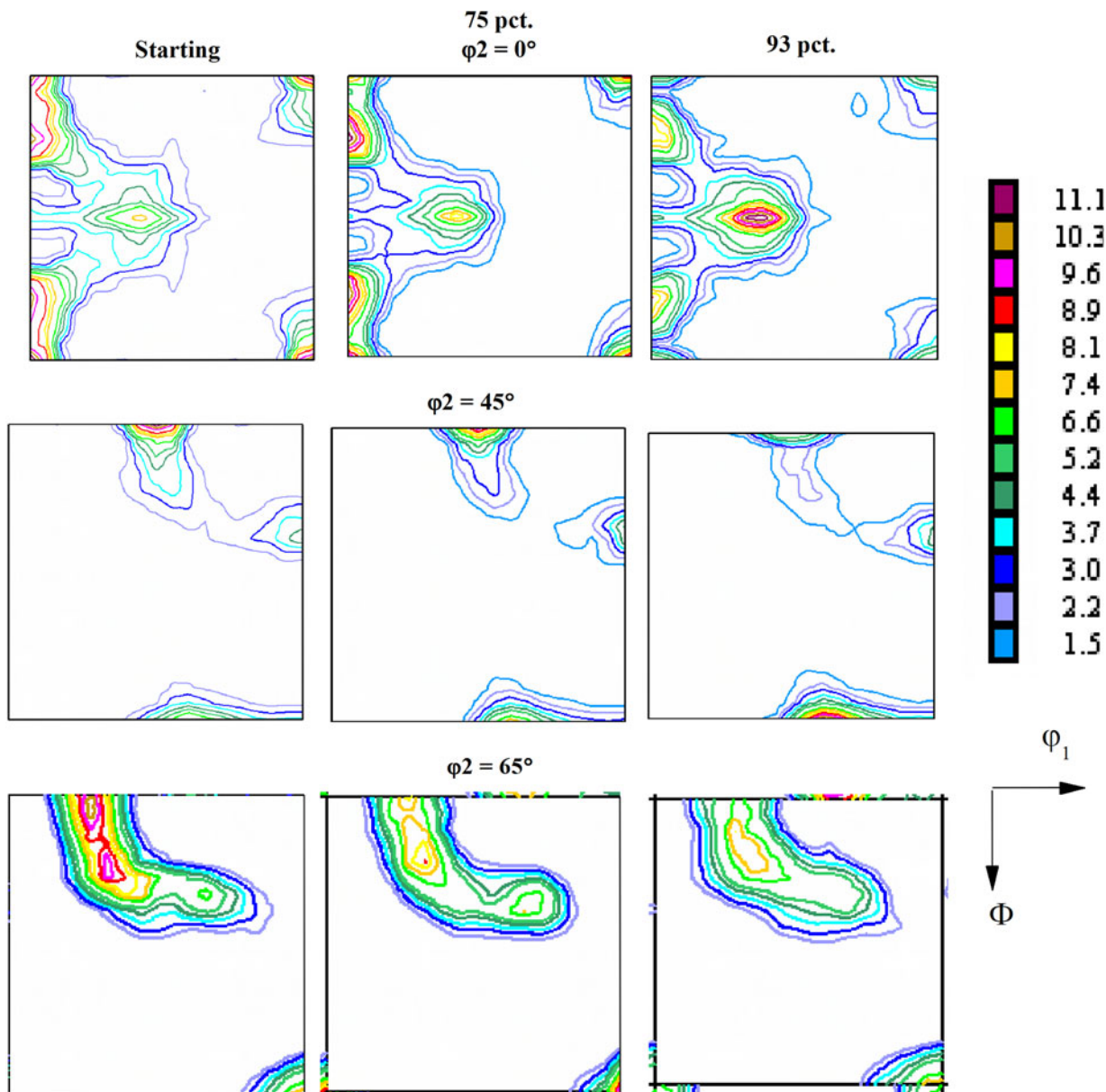


Fig. 7— $\phi_2 = 0, 45,$ and 65 deg sections of the ODF for that starting material, and for deformed Cu-Cu multilayers with rolling reductions of 75 and 93 pct. The major texture components are Bs, S, RD-cube, Cu, and cube.

during DRX, (iii) stability of rotated cube component during deformation, and (iv) high amount of Bs during deformation. To validate the above statements, the EBSD results were partitioned as deformed and recrystallized grains based on GOS values. Since, GOS is an indirect measure of strain, grain with low GOS values will mostly contain recrystallized grains and grain with high GOS values are mostly deformed grains. The partitioned microstructures, along with the corresponding crystallographic texture comprising $\phi_2 = 0, 45,$ and 65 deg sections of the ODF, are shown in Figure 12. Textures for grains with $GOS > 3$ exhibit strong a RD-cube component, whereas grains with $GOS < 2$ show strong cube with minimal spread about the RD. Additionally, grains with $GOS < 2$ exhibit strong Bs in all conditions and an increasing Cu and S intensity with

strain and grains with $GOS > 3$ show high Bs and low Cu and S.

B. Dynamic Recrystallization

High fraction of VLABs compared with LAB denote concomitant occurrence of restoration process along with the deformation. Copper is a well-known cell forming metal and high fractions of VLABs could be associated with cell formation.^[26] The IPF maps of all the rolled material, Figure 1, show some regions of very low intra grain misorientation and strain-induced boundary migration (SIBM) is one possible mechanism that could lead to such variations in content. The partitioning of microstructures on the basis of GOS values, Figure 12, indicates that at lower deformation

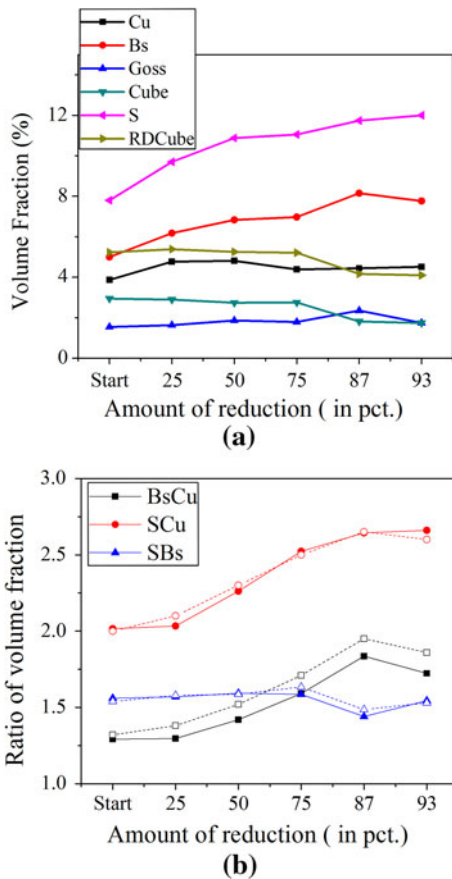


Fig. 8—Volume fraction of different fcc texture components and ratio of texture components of deformed Cu-Cu multilayer.

levels, the texture is characterized by strong cube, and that with increasing deformation, the characteristic deformation texture is mostly retained in regions with low misorientation gradient. Because CDRX does not lead to a profound change in characteristic deformation texture,^[35,36] this seems to be one of the major restoration processes. After 75 pct rolling reduction, a large fraction of them possess orientations that are entirely different from the neighboring grains and have low GAM and KAM values. With further increase in strain, especially at 83 pct deformation, most of the grains are equiaxed (Figure 13). The TEM micrograph in Figure 13(b) displays Moiré fringes having characteristic features of low dislocation density in along the grain boundary region, which could be from a low angle grain boundary. The bright-field and dark-field TEM images suggest grain sizes of about 80 nm. The interlayer interface can act as a transition band where large strains can be accumulated, which leads to the formation of new strain free grains. Therefore, a transition from continuous to DDRX appears to initiate at 50 pct deformation. The presence of a strong cube component in partitioned microstructures with GOS < 2.0 also confirms the occurrence of DDRX. Although the DDRX process initiates after 50 pct deformation itself, it does not lead to the formation of additional annealing twins (in the sense that the annealed 75 pct material has

the same $\Sigma 3$ content as the starting material). Furthermore, not all the large grains possess low intra-grain misorientation, which suggests the occurrence of an additional mechanism that leads to grain growth with larger intra-grain misorientation in addition to SIBM. Grain rotation induced grain coalescence could be a possible mechanism. The grain size distribution exhibits a significant fraction of very large grain sizes, which increase beyond the layer thickness; such a distribution confirms abnormal subgrain growth during each stage of the multilayer deformation. However, the tendency for abnormal subgrain growth decreases at larger strains, which is confirmed by a unimodal grain size distribution with a large fraction of HAB. This lower tendency for abnormal subgrain growth could be attributed to lowering of stored energy in the system through higher activation of dynamic recrystallization processes and a more uniform deformation condition.

C. Restricted Grain Growth

The diverse nature of the grain size distribution of the annealed samples largely depends on the prior strain, which is quite evident from the grain size distribution given in Figure 5. The origin for such heterogeneity is likely a consequence of two competing effects. Although the regions surrounding the thin oxide layers result in very fine grain sizes, abnormal grain growth of mostly cube-oriented grains tends to coarsen the grain structure. The second effect is discussed in the following section. Formation of a fine-grained structure surrounding the thin oxide layer could be the result of either low grain boundary mobility across the oxide layer or low activation barrier to form new recrystallized grains. In order to understand the evolution of such fine grained microstructure surrounding the oxide layers, they were partitioned and the corresponding texture are presented in Figure 14 for the extreme conditions (for which EBSD maps were available) namely the annealed conditions of the starting and 75-pct-deformed materials. The fine grains corresponding to starting material display a strong RD-cube component. Strong Cu and Bs components were observed in the case of annealing of the heavily rolled sample. Both these findings indicate that presence of such a fine oxide layer could restrict the annealing process to retain the deformation texture. Such type of restricted annealing has also been reported in Cu-Nb multilayer.^[11]

D. Abnormal Grain Growth

As discussed earlier, the annealed microstructure does not represent a uniform trend in the average grain size with respect to the applied strain. This discrepancy could be attributed to the differences in stored energy of the deformed samples, which did not increase linearly with strain. Moreover, the grain size distribution changes from a unimodal distribution for the starting material to bimodal distribution for 75-pct-deformed sample after annealing. As stated earlier, the grain coalescence due to grain rotation does not lead to a lower intra-grain misorientation and such types of grain

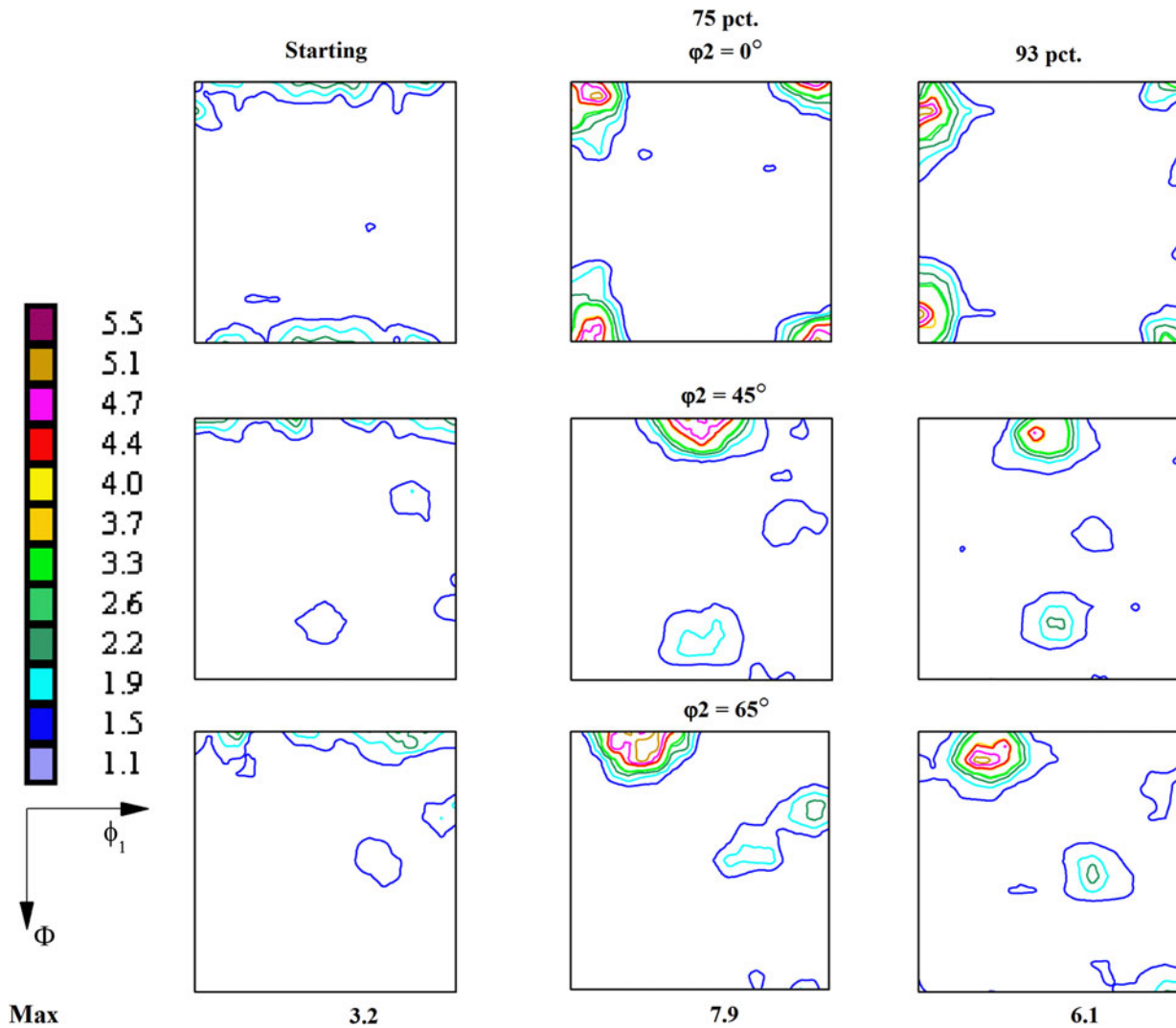


Fig. 9— $\phi_2 = 0, 45,$ and 65 deg sections of the ODF of annealed Cu-Cu multilayers for the starting material along with 75 and 93 pct rolling reductions. The annealing of starting material is quite weak compared with other deformation conditions. The dominant components are cube and BR (80, 31, and 35 deg).

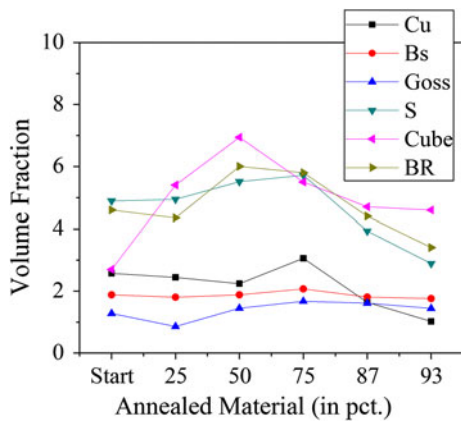


Fig. 10—Volume fraction of important fcc texture components of annealed Cu-Cu Multilayers.

generally have a higher tendency for grain growth compared with other grains and can form larger grains. Since the growth of the grains is mostly restricted across the interfaces in the multilayer, they have a tendency to grow parallel to the rolling direction and this leads to higher aspect ratios in grain shape. Hence, recrystallization occurs in a constricted manner. This is also supported by the fact that annealing of 75-pct-deformed samples leads to a lower CSL fraction and a higher low angle boundary fraction.

E. Evolution and Stability of Some Texture Components

1. Evolution of Bs in deformed multilayers

The texture observations from both bulk X-ray texture measurement and micro-texture from EBSD reveal a higher fraction of Bs component compared with the Cu component. Cu having a moderate SFE of

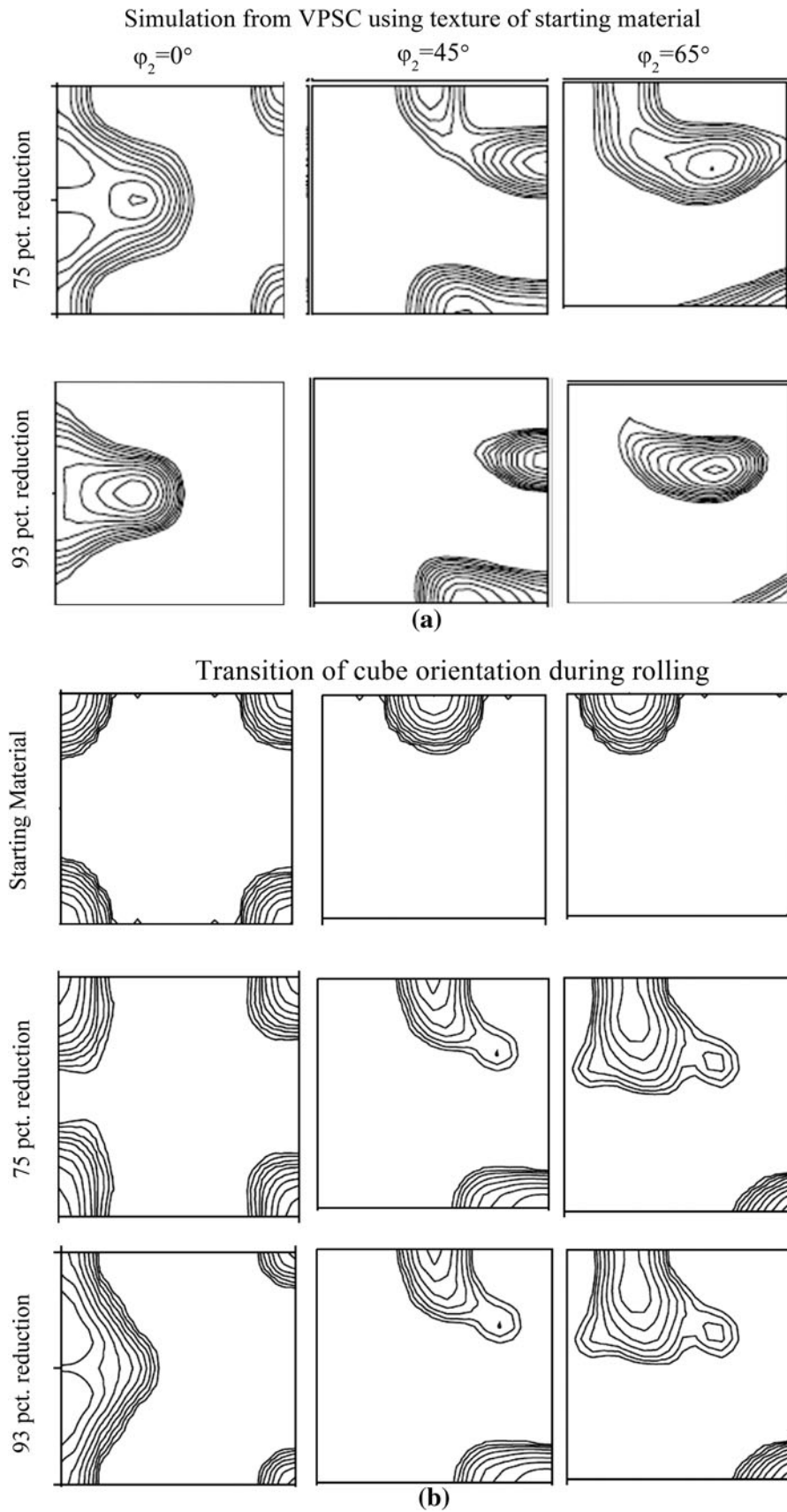


Fig. 11— $\phi_2 = 0, 45,$ and 65 deg sections of ODF obtained through VPSC simulations (a) for 75 and 93 pct reduction and (b) change in cube orientation during rolling. Iso intensity levels corresponds to 1.0 1.3 1.6 2.0 2.5 3.2 4.0 5.0 6.2.

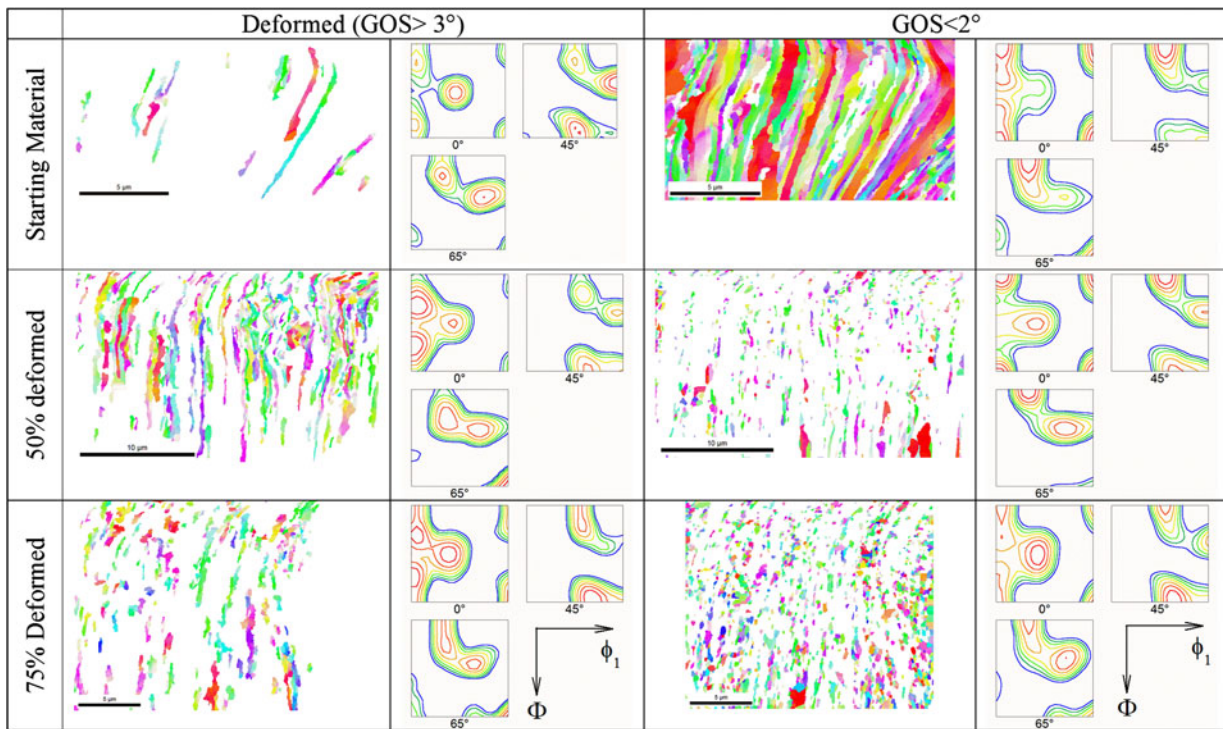


Fig. 12—Inverse pole figure and ODF sections ($\phi_2 = 0, 45,$ and 65 deg) for the data partitioned into regions with $GOS > 3$ and $GOS < 2$. Up to 50 pct reduction, texture is characteristically different for tow partitioned regions, and after 75 pct reduction both the partitioned grains exhibit similar texture.

$\sim 80 \text{ mJ/m}^2$ is expected to develop a strong Cu compared with Bs.^[26,31] One of the early observations of high Bs component in a coarse grained high SFE material was made by Dolland and Nes in Reference 37 who reported higher Bs component during cold rolling of directionally solidified Al. Its origin was related to the rotation of pre-existing Goss-oriented grains. In the current case, the volume fraction of Goss is consistently low. Other deformation mechanisms that could lead to higher fractions of Bs in medium as well as high SFE materials are as follows: (i) profuse twinning, (ii) planar slip, (iii) shear band formation, and, (iv) large aspect ratio of grains.^[38] None of the microstructural observations show deformation twins, however. Various discussions^[39–41] on the effect of grain size on the activation volume for cross slip have suggested that restriction of cross slip and a predominant occurrence of planar slip would take place in the grain size regime of ~ 15 to 50 nm . In the current investigation, the average grain size is at least two times larger than the maximum limit. So, planar slip is unlikely to explain our observations. During the initial stages of rolling, shear band formation was observed which at later stages decreased. Since the layer thickness is very small (~ 40 to $250 \text{ }\mu\text{m}$), the effect of friction on the material can be quite significant. Previous studies^[42–44] on through thickness texture gradient in IF steel and Al have shown that surface and subsurface texture have the maximum contribution from surface shear compared with the center. In particular, during conventional rolling of AA5182 alloy, the surface layer exhibited a higher fraction of Bs

component compared with the middle layer.^[45] However, the authors did not make any note on this particular aspect. Similarly, Engler *et al.*^[43] in their study of through thickness texture variation of commercial-purity Al (AA1145) found that Bs was stronger in the surface. In the current study, owing to the very small layer thickness (40 to $500 \text{ }\mu\text{m}$), the ratio of the contact length between the roll and sample to the sample thickness varies between 10 and 25. The effect of shear was found to be dominant for ratios greater than one and in such conditions shear texture develops at a faster rate compared with the rolling texture. In addition to the frictional effects, large grain aspect ratio itself could lead to the formation of Bs. Lebensohn and Leffers have shown that for very large grain aspect ratio, owing to the effects of strain relaxation, Bs texture develops.^[46] During initial stages of deformation, the relaxation of strain terms, the large grain aspect ratio from the prior ARB could aid in the formation of Bs, which at later stages is dominated by the frictional effects.

2. Evolution of RD-cube component in deformed layers

Recrystallization of cold rolled Cu leads to the formation of strong cube component and materials with high fractions of Bs component develop Goss and/or BR component after annealing.^[26] The dynamic recrystallization that is prevalent from the microstructural studies does not lead to a Goss component from the deformed Bs. Rather it tends to produce strong cube and RD-Cube, along with a weak BR. The cube component in the starting material could be attributed

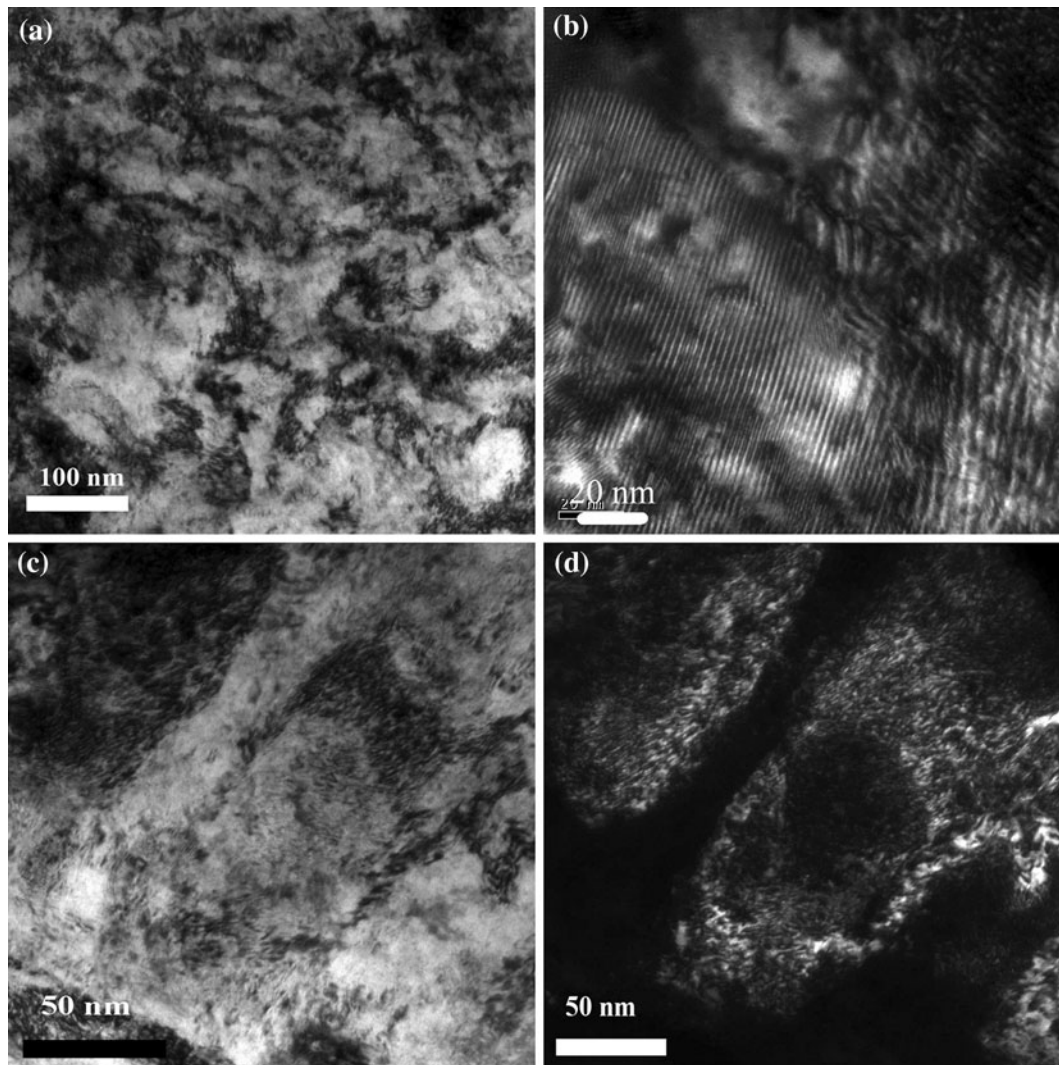


Fig. 13—TEM micrographs of 87-pct-deformed sample. (b) Moiré fringes display regions with low dislocation density along grain boundary. (c) Bright-field and (d) dark-field images of the micrograph suggest the approximate grain size as 80 nm.

to the dynamic recrystallization mechanism that occurs during the prior hot rolling process. Despite a 50 pct reduction in each successive pass, these cube-related components maintain their strength during the cold rolling processes. In general, for rolled fcc materials, the cube component is unstable during the cold deformation process. In the current study, the RD-cube component exhibits a higher volume fraction compared with the cube and its intensity is nearly constant throughout the cold rolling. Stability of the cube component during hot rolling of various Al alloys has been reported.^[47–50] This stability has been discussed based on either the survival of old cube-oriented grain or the formation of new cube-oriented grains. Raabe *et al.*^[49] showed that, at very high friction values, plane strain compression leads to large spread in the cube grains. As stated earlier, because of the very small layer thickness, the friction between the sample and roll surface can play a major role in changing the texture. In addition, the friction between the bonded layers can also have an impact on the deformation mechanism. The microstructures with high

GOS regions display RD-cube, which suggests that they are a result of deformation.

V. CONCLUSIONS

The microstructure and texture evolved during rolling and annealing of ARB-processed Cu-Cu multilayers were studied. The main results of current study are as follows:

1. During deformation, restoration processes such as CDRX and DDRX are active. DDRX starts at later stages of deformation. The influence of CDRX is greater than that of DDRX.
2. The high strength of the Bs component during deformation is attributed to the large initial grain aspect ratio and frictional effects. The RD-cube component is present throughout the deformation.
3. Constricted annealing and abnormal grain growth lead to bimodal grain size distributions.

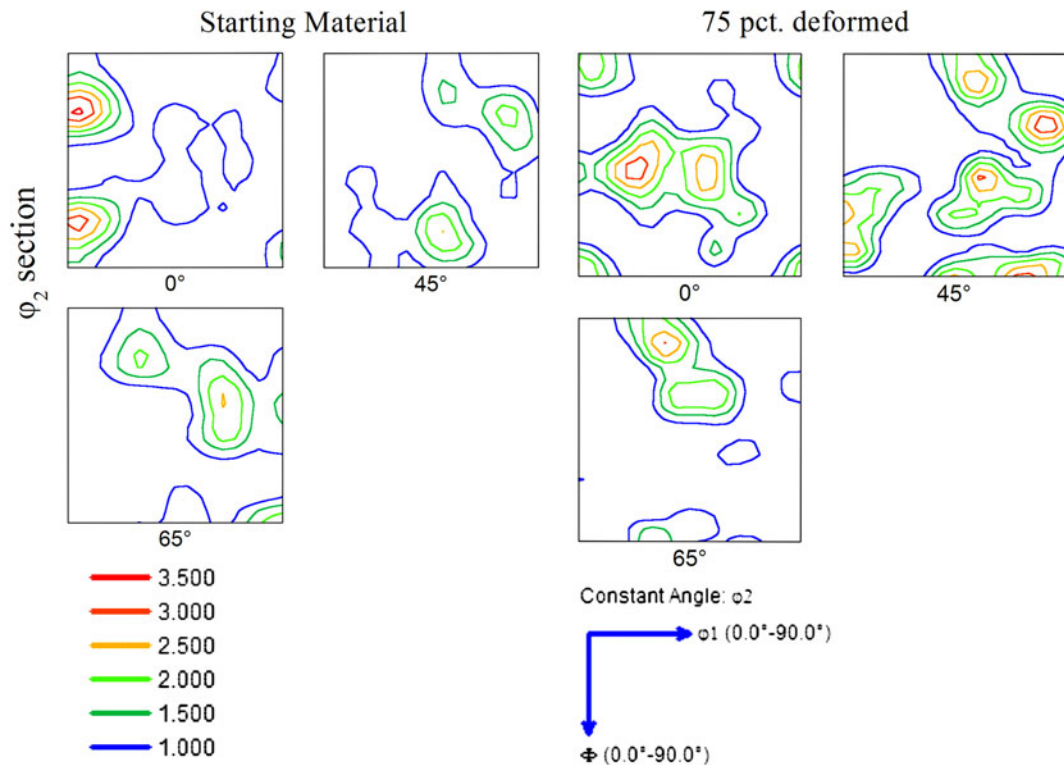


Fig. 14—ODF sections ($\phi_2 = 0, 45,$ and 65 deg) for the fine grains surrounding thin oxide interface in annealed material. Formation of Bs and Cu components during later stages of deformation (at regions surrounding the oxide layer) indicate constrained annealing.

4. The annealing textures are dominated by oriented nucleation.

ACKNOWLEDGMENTS

One of the authors (SS) acknowledges the fellowship awarded by Indo-US Science and Technology Forum (IUSSTF) during which current study was initiated. Most of the experiments were carried out at the Institute X-ray facility and Advanced facility for microscopy and microanalysis (AFMM) at IISc, Bangalore. A part of the current study was supported through a grant from the Department of Science and Technology, Government of India. ADR acknowledges the support provided in part by the Center for Materials at the Irradiation and Mechanical Extremes, an Energy Frontier Research Center funded by the U.S. Department of Energy, the Office of Science, and the Office of Basic Energy Sciences, in addition to the support of the Department of Materials Engineering at IISc through the Brahm Prakash Chair Professorship.

REFERENCES

1. L.H. Friedman: *Scripta Mater.*, 2004, vol. 50, pp. 763–67.
2. F. Spaepen and D.Y.W. Yu: *Scripta Mater.*, 2004, vol. 50, pp. 729–32.
3. R.G. Hoagland, R.J. Kurtz, and C.H. Henager: *Scripta Mater.*, 2004, vol. 50, pp. 775–79.
4. R.G. Hoagland, T.E. Mitchell, J.P. Hirth, and H. Kung: *Phil. Mag.*, 2002, vol. 82, pp. 643–64.

5. W.D. Nix: *Scripta Mater.*, 1998, vol. 39, pp. 545–54.
6. K.O. Schweitz, J. Chevallier, J. Bottiger, W. Matz, and N. Schell: *Phil. Mag. A*, 2001, vol. 81, pp. 2021–32.
7. P.M. Anderson, J.F. Bingert, A. Misra, and J.P. Hirth: *Acta Mater.*, 2003, vol. 51, pp. 6059–75.
8. Y. Jyoko, S. Kashiwabara, and Y. Hayashi: *J. Electrochem. Soc.*, 1997, vol. 144, pp. L5–L8.
9. I.J. Beyerlein, N.A. Mara, D. Bhattacharyya, D.J. Alexander, and C.T. Necker: *Int. J. Plast.*, 2011, vol. 27, pp. 121–46.
10. J. Wang, I.J. Beyerlein, N.A. Mara, and D. Bhattacharyya: *Scripta Mater.*, 2011, vol. 64, pp. 1083–86.
11. S.C.V. Lim and A.D. Rollett: *Mater. Sci. Eng. A*, 2009, vol. 520, pp. 189–96.
12. Y. Saito, H. Utsunomiya, N. Tsuji, and T. Sakai: *Acta Mater.*, 1999, vol. 47, pp. 579–83.
13. N. Tsuji, Y. Ito, Y. Saito, and Y. Minamino: *Scripta Mater.*, 2002, vol. 47, pp. 893–99.
14. H. Sieber, J.S. Park, J. Weissmüller, and J.H. Perepezko: *Acta Mater.*, 2001, vol. 49, pp. 1139–51.
15. H. Chang, M.Y. Zheng, W.M. Gan, K. Wu, E. Maawad, and H.G. Brokmeier: *Scripta Mater.*, 2009, vol. 61, pp. 717–20.
16. L. Chen, Q. Shi, D. Chen, S. Zhou, J. Wang, and X. Luo: *Mater. Sci. Eng. A*, 2009, vol. 508, pp. 37–42.
17. M. Shaarraf and M.R. Toroghinejad: *Metall. Mater. Trans. A*, 2009, vol. 40A, pp. 1693–700.
18. S.A. Hosseini and H. Danesh Manesh: *Mater. Des.*, 2009, vol. 30, pp. 2911–18.
19. M. Shaarraf and M.R. Toroghinejad: *Mater. Sci. Eng. A*, 2008, vol. 473, pp. 28–33.
20. S. Roy, S. Singh, S. Suwas, S. Kumar, and K. Chattopadhyay: *Mater. Sci. Eng. A*, 2011, vol. 528, pp. 8469–78.
21. Y. Wang, M. Chen, F. Zhou, and E. Ma: *Nature*, 2002, vol. 419, pp. 912–15.
22. Y.-H. Zhao, X.-Z. Liao, S. Cheng, E. Ma, and Y.T. Zhu: *Adv. Mater.*, 2006, vol. 18, pp. 2280–83.
23. E. Ma: *Scripta Mater.*, 2003, vol. 49, pp. 663–68.
24. N. Takata, S.-H. Lee, and N. Tsuji: *Mater. Lett.*, 2009, vol. 63, pp. 1757–60.

25. J.-Y. Cho, K. Mirpuri, D.N. Lee, J.-K. An, and J.A. Szpunar: *J. Electron. Mater.*, 2005, vol. 34, pp. 53–61.
26. F.J. Humphreys and M. Hatherly: *Recrystallization and Related Annealing Phenomena*, Elsevier, Oxford, 2004.
27. D.P. Field, D. Dornisch, and H.H. Tong: *Scripta Mater.*, 2001, vol. 45, pp. 1069–75.
28. K.N. Tu: *J. Appl. Phys.*, 2003, vol. 94, pp. 5451–73.
29. K.S. Suresh, S. Sinha, A. Chaudhary, and S. Suwas: *Mater. Charact.*, 2012, vol. 70, pp. 74–82.
30. K. Pawlik, J. Pospiech, and K. Lücke: *Texture and Microstructures*, 1991, vol. 25, pp. 14–18.
31. F. Kocks, H.-R. Wenk, and C.N. Tomé: *Texture and Anisotropy*, Cambridge University Press, Cambridge, 1998, pp. 473–80.
32. C.N. Tomé and R.A. Lebensohn: *Manual for visco plastic self consistent*, version 7B, 2007.
33. V. Randle and O. Engler: *Introduction to texture analysis*, CRC Press, 2002.
34. J. Hirsch, E. Nes, and K. Lücke: *Acta Metall.*, 1998, vol. 35, p. 427438.
35. H. Jazaeri and F.J. Humphreys: *Acta Mater.*, 2004, vol. 52, pp. 3239–50.
36. H. Jazaeri and F.J. Humphreys: *Acta Mater.*, 2004, vol. 52, pp. 3251–62.
37. O. Dolland and E. Nes: *Acta Mater.*, 1996, vol. 44, pp. 1389–1411.
38. T. Leffers and R.K. Ray: *Prog. Mater. Sci.*, 2009, vol. 54, pp. 351–96.
39. P. Rodriguez: *Metall. Mater. Trans. A*, 2004, vol. 35A, pp. 2697–2705.
40. T. Narytani and J. Takamura: *Acta Metall. Mater.*, 1991, vol. 227, pp. 2037–49.
41. N.P. Gurao and S. Suwas: *App. Phys. Lett.*, 2004, vol. 94, p. 191902.
42. O.V. Mishin, B. Bay, and D. Juul Jensen: *Metall. Mater. Trans. A*, 2000, vol. 31A, pp. 1653–62.
43. O. Engler, M.-Y. Huh, and C.N. Tome: *Metall. Mater. Trans. A*, 2000, vol. 31A, pp. 2299–315.
44. W.C. Liu and J.G. Morris: *Metall. Mater. Trans. A*, 2005, vol. 36A, pp. 1329–38.
45. C.I. Maurice and J.H. Driver: *Acta Mater.*, 1997, vol. 45, pp. 4627–38.
46. R. Lebehnon and T. Leffers: *Texture Microstruct.*, 1999, vol. 31, pp. 217–30.
47. M.H. Alvi, S.W. Cheong, J.P. Suni, H. Weiland, and A.D. Rollett: *Acta Mater.*, 2008, vol. 56, pp. 3098–3108.
48. L. Delannay, O.V. Mishin, D. Juul Jensen, and P. Van Houtte: *Acta Mater.*, 2001, vol. 49, pp. 2441–51.
49. D. Raabe, Z. Zhao, and F. Roters: *Scripta Mater.*, 2004, vol. 50, pp. 1085–90.
50. H.E. Vatne, R. Sahani, and E. Nes: *Acta Mater.*, 1996, vol. 44, p. 4447.